Frequency modulated (FM) time delay photoacoustic and photothermal wave spectroscopies. Technique, instrumentation, and detection. Part II: Mirage effect spectrometer design and performance

Andreas Mandelis and Linda M. L. Borm

Photoacoustic and Photothermal Sciences Laboratory, Department of Mechanical Engineering, University of Toronto, Toronto, Ontario M5S 1A4, Canada

John Tiessinga

Research Laboratory, West Tower, Ministry of Transportation and Communications, Downsview, Ontario M3M 1J8, Canada

(Received 14 October 1985; accepted for publication 2 December 1985)

FM time delay laser excitation has been implemented in a photothermal deflection spectrometric apparatus with fast rise-time optics. The performance of the system was studied in both frequency and time delay domains. The spectrometer was further used in the study of thin quartz layers on an opaque substrate. In this work we have demonstrated the operation of the first frequency modulated (FM) time delay photothermal deflection (mirage effect) spectrometer with a ns rise time spectrally flat beam position detector unit. It was established by use of a blackbody reference that the spectrometer is responsive to impulsive heat sources in the sample with no measureable instrumental distortion of the frequency or time delay domain responses. The sensitivity of the device was tested successfully in the measurement of thermal parameters of thin quartz layers on absorbing backings. It was further shown that our spectrometer is sensitive to thin SiO_2 layers on Si wafers. The data were largely consistent with Green's function models of heat conduction in the liquid interface and bulk. The ability of the spectrometer to perform high-quality frequency response measurements via fast Fourier transformations of the input data in very short time compared to the conventional lock-in detection is an extremely useful feature for thermal-wave applications.

INTRODUCTION

In Part I of this work it was shown that the FM time delay technique can be used to give photoacoustic or photothermal wave signals mathematically equivalent to the impulse response of a sample, provided that the autospectrum of the input signal $X(t)$ is uniform throughout the frequency range of the experiment. This criterion can be achieved, in practice, if the total sweep time is long compared to the time delayed response of the system. In order to take full advantage of the simplicity of interpretation of the impulse response signal, it is imperative to use a photothermal apparatus with a flat frequency response from dc up to frequencies well above the highest experimental frequency. In conventional photoacoustic spectroscopy (PAS) microphone transducers are used in the vicinity of the sample in order to monitor the pressure increase due to thermal expansion in the gas at the gas–sample interface, following light absorption and conversion of a fraction of the optical energy into heat via nonradiative mechanisms.[1] Unfortunately, microphones, albeit very sensitive transducers, have a rather narrow flat frequency response, typically in the range[2] between 20 Hz and 5–10 kHz. Excursions from microphone frequency response linearity have been shown to contribute additional time delays to the time-domain photoacoustic signal,[3] and have been suspected as the main source of discrepancy between experimental data and theory in the optical absorption coefficient-dependent calculation of delay times in cross-correlation photoacoustic spectroscopy (CPAS).[4] Similar hard to interpret time delays in CPAS system characterization have been reported by Sugitani *et al.*[5]

The conventional apparatus employed in photothermal deflection (mirage effect) spectroscopic studies (PDS) makes use of bicell or quadrant position sensors capable of detecting minute deflections of probe laser beams due to thermal modulation of the fluid refractive index near the solid sample–fluid interface, following optical heating of the sample surface.[6,7] Position sensors are typically[8] band limited between dc and 2 kHz and, therefore, they present problems similar to those encountered with PAS and CPAS. Piezoelectric transducers are wide-band detectors, however, mechanical resonances introduce undesirable nonlinearities in the frequency response, which could distort the time delay domain signal.[9]

In this work we present for the first time a FM time delay domain photothermal deflection spectrometer based on the theoretical principles of Part I, with a flat detector frequency response between dc and tens of MHz. The performance of the spectrometer was studied using a blackbody reference sample in water, as well as thin quartz films of variable thickness. The experimental results were further compared with impulse–response generating models using Green's function formulations of the thermal wave problem.

 0034-6748/86/040622-08$01.30

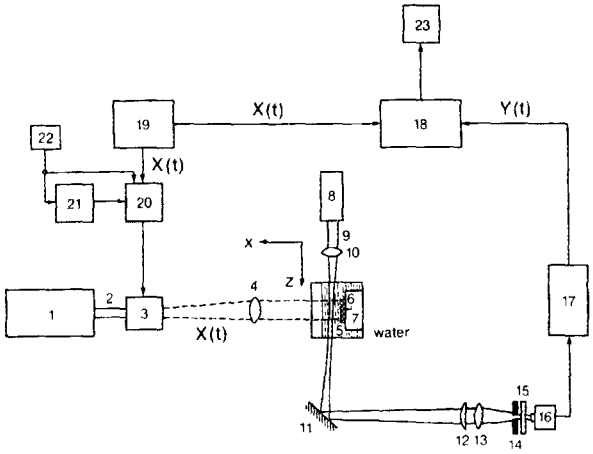

FIG. 1. FM time delay mirage effect spectrometer; 1: Nd^{3+}:YAG pump laser; 2: cw 1.06-μm beam; 3: acousto-optic (A/O) modulator; 4: alignment lens; 5: water; 6: sample; 7: sample holder; 8: He–Ne probe laser; 9: 632.8-nm probe beam; 10: focusing lens; 11: optical lever reflector mirror; 12, 13: lenses; 14: 50-μm-diam pinhole; 15: He–Ne beam interference filter; 16: fast rise-time photodiode; 17: wide bandwidth preamplifier; 18: dual channel FFT analyzer; 19: synthesizer/function generator; 20: A/O modulator driver; 21: A/O driver power amplifier; 22: A/O modulator power supply; 23: computer memory storage. See text for more details. $X(t)$ and $Y(t)$ are identified with system functions using the same symbols as in Part I.

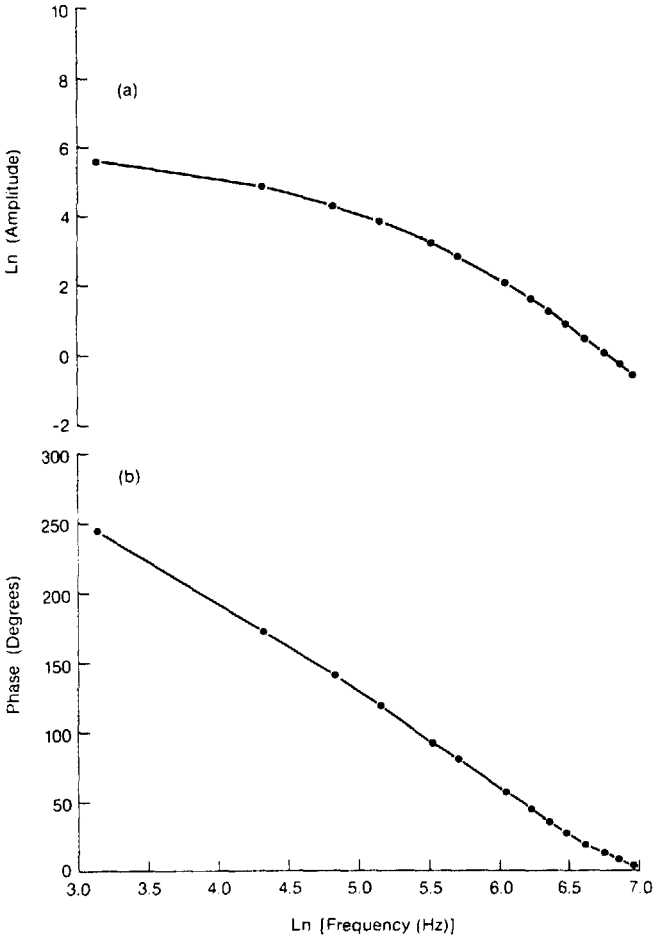

FIG. 2. Experimental dependence of detector signal on modulation frequency. (a) Amplitude; (b) phase.

I. APPARATUS AND CHARACTERIZATION

Our time delay domain apparatus is shown in Fig. 1. The heart of the system consists of a Hewlett–Packard Model 3325A synthesizer/function generator (#19 in Fig. 1) operating in the frequency sweep mode and driving an Isomet model 1201E acousto-optic (A/O) modulator at 1.06 μm input wavelength from a 2-W Nd^{3+}:YAG pump laser. The deflection of the transverse[6] probe He–Ne laser beam focused above the sample surface was enhanced in the presence of water due to the higher refractive index gradient $\partial n/\partial T$ of the latter than that of air.[10] The FM pump laser beam was expanded over a large area of the sample surface compared to the probe beam waist, in order to facilitate the theoretical interpretation of the data. The deflections of the probe beam were converted to intensity variations using a combination of lenses, a pinhole, and a photodiode as the detector unit, Fig. 1. The infinitely flat frequency response of the pinhole together with the fast rise time of the photodiode (Silicon Detector Corporation, photovoltaic diode model SD-100-12-12-021 with a 34-ns response time) provided an ideally flat detector from dc up to $\sim$30 MHz. The preamplified signals were fed into the input channel B of a Nicolet Scientific Corp. model 660A dual channel FFT analyzer. The input channel A of this device was connected to the linear frequency sweep generator. All the necessary frequency and time delay domain functions were calculated via the FFT analyzer. The system input signal $X(t)$ was modulation-depth optimized by adjusting the peak-to-peak voltage applied to the A/O modulator to $\sim$0.8 V. This signal was available as a reference channel sync output of the HP 3325A synthesizer/function generator.

The characterization of the system consisted in showing that its response to a single-frequency harmonic excitation was consistent with the well-known behavior of conventional mirage effect systems[6,11] employing band-limited beam position detectors. For this purpose, a sinusoidal input voltage was used to drive the A/O modulator and the PDS signal from our detector unit was fed into an EG&G Princeton applied research model 5204 lock-in analyzer. Figure 2 shows the modulation frequency dependence of the PDS amplitude and phase for a beam offset $x_0 \cong 60\,\mu$m. The sample used was black anodized aluminum in water. The fast exponential dropoff of the amplitude with frequency in Fig. 2(a) is proportional to $\exp(-x_0/\mu_f)$, as expected,[6,11] where $\mu_f = (2\alpha_f/\omega_0)^{1/2}$ is the thermal diffusion length in the water at ω_0 and α_f is the thermal diffusivity of water. The approximately linear dependence of the PDS phase on the logarithm of frequency in Fig. 2(b) is also consistent with one-dimensional theoretical considerations.[11] Further measurements on the dependence of the PDS signal on the Nd^{3+}:YAG input beam intensity were performed using neutral density filters of variable transmittance. The results are shown in Fig. 3. The signal amplitude, Fig. 3(a), is essentially linear up to beam intensities of $\sim$600 mW and exhibits the onset of saturation at higher intensities. The signal phase, Fig. 3(b), appears to be independent of input beam intensity. The linear response region of Fig. 3(a) and the flat phase are in agreement with elementary theoretical considerations of the

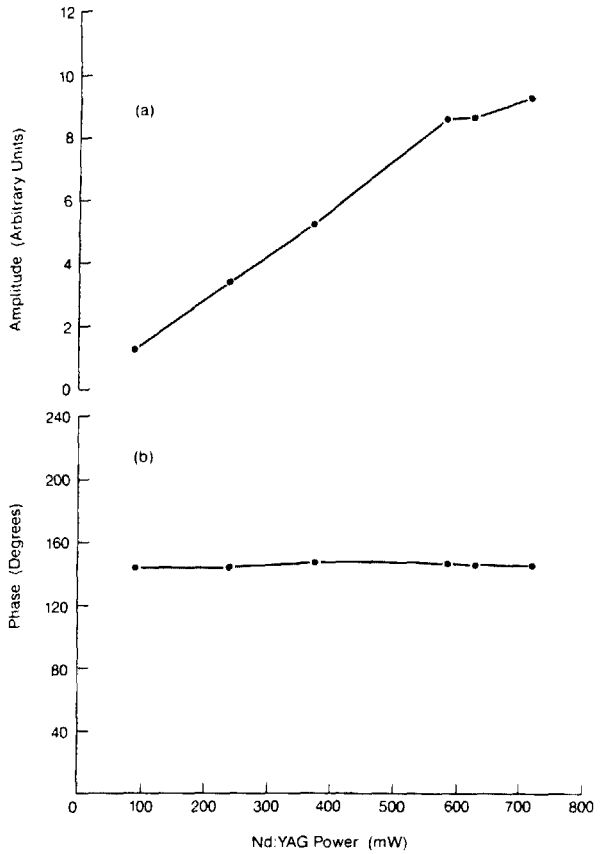

FIG. 3. Experimental dependence of detector signal on pump laser intensity at $f = 25$ Hz and $x_0 = 0.1$ mm. (a) Amplitude; (b) phase.

physics of the PDS signal generation.[6,11] To explain the saturation region of Fig. 3(a) the nature of the detector unit must be invoked, namely the fact that the photodiode detects the integrated probe beam light intensity over the area A of the pinhole. Directly behind the pinhole of radius a the intensity is

$$P(a) = \frac{1}{2\eta} \int\int_A |E(a)|^2 dA , \tag{1}$$

where E is the electric field vector of the transmitted probe beam radiation and η is the free-space impedance. For a Gaussian laser beam deflected by x_a from its offset position x_0 due to the mirage effect, we can write

$$E^2 = E_0^2 \exp[-2r^2(\theta)/W_0^2] , \tag{2}$$

where W_0 is the beam spotsize at the pinhole and, assuming a circular aperture with the beam centroid at its center when $x_a = 0$

$$r^2(\theta) = a^2 + x_a^2 - 2ax_a \cos\theta . \tag{3}$$

Using Eqs. (2) and (3) in (1) gives

$$P(a) = \frac{E_0^2}{2\eta} \int_0^{\pi} d\theta \int_0^{r(\theta)} e^{-2y^2/W_0^2} y\, dy . \tag{4}$$

For small pinhole diameter to spotsize ratios, Eq. (4) becomes

$$P(a) \cong (W_0^2\pi/2)P_0\{1 - \exp[-2(x_a^2 + a^2)/W_0^2]\} , \tag{5}$$

where P_0 is the input intensity. In our experiments ($a/W_0 \cong 0.25$. The deflection x_a can be calculated from the paraxial ray equation[12]

$$n_0 \frac{\partial^2}{\partial z^2} x_a(z, \omega_0) = -\frac{\partial}{\partial x} n(x, \omega_0)\Big|_{x = x_a(z, \omega_0)} . \tag{6}$$

In Eq. (6), z and x are directions shown in Fig. 1, and $n(x, \omega_0)$ is the refractive index in the water. Expanding $n(x, \omega_0)$ in the Taylor form

$$n(x, \omega_0) = n_0 + \left(\frac{\partial n}{\partial T}\right)_{T = T_0} T_f(x, \omega_0) , \tag{7}$$

where $T_f(x, \omega_0)$ is the fluid temperature profile, and using Eq. (4), Ref. 13 for T_f gives the probe beam deflection as a function of distance z along the sample–fluid interface

$$x_a(z) = B \cos[(\sqrt{2}\, I_0\omega_0/\alpha_f n_0)^{1/2} e^{i\pi/8} z] , \tag{8}$$

$$I_0 \equiv \left(\frac{\partial n}{\partial T}\right)_{T = T_0} \frac{P_0}{4\alpha_s k_s} . \tag{9}$$

α_s, k_s are the thermal diffusivity and conductivity of the sample, respectively, and B is a constant independent of P_0. Notice that a constant (i.e., P_0 independent) term in the solution of Eq. (6) was omitted from (9) for simplicity. A combination of Eqs. (5) and (8) shows that, as long as $x_a \ll W_0$, i.e., for

$$I_0 \ll (\alpha_f n_0/\sqrt{2}\,\omega_0)^{1/2}/z, \quad P(a) \propto P_0$$

as expected from the conventional theory. For higher inten-

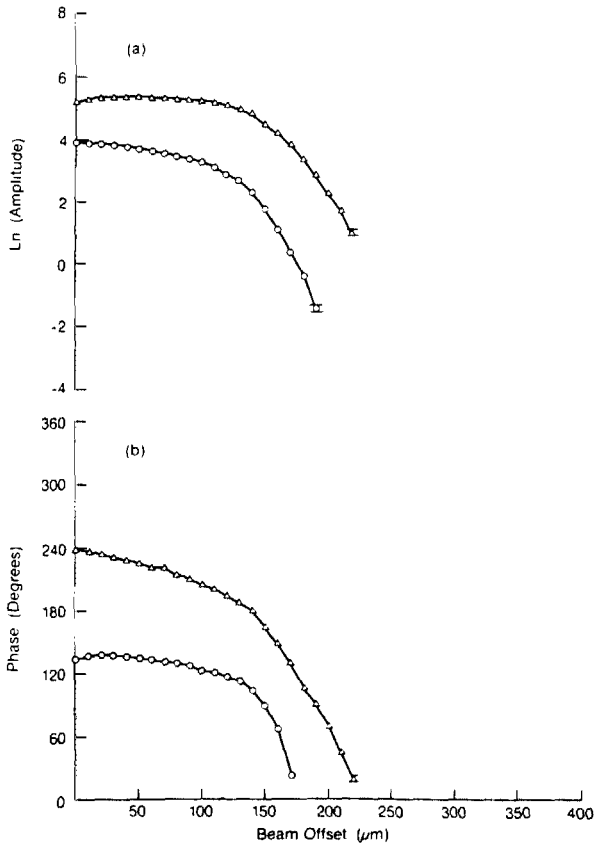

FIG. 4. Experimental dependence of detector signal on beam offset at 25 Hz (-Δ-) and 140 Hz (-O-). (a) Amplitude; (b) phase.

sities, however,

$$P(a) \propto P_0\{1 - \exp[-2(a/W_0)^2] \times \exp[-(B/W_0^2)\cos(GP_0^{1/2})]\}$$

and the output signal will exhibit saturation for values of P_0 such that the second term in the brackets becomes comparable to unity. The above considerations with $z = 1$ cm and $\omega_0 = 2\pi \times (25\ \text{Hz})$ give

$$P_0 \ll 300\ \text{mW}$$

as the condition for linearity in Fig. 3(a), consistent with the data presented in that figure. The phase of the signal, Eq. (8), is seen to remain constant in crossing the low P_0 to high P_0 regime, in agreement with Fig. 3(b).

Finally, signal versus probe beam offset data are shown in Fig. 4 for two modulation frequencies. The flatness of both amplitude and phase curves for offsets below $\sim 100\ \mu$m is due to the partial screening of the beam by the sample. The approximately linear behavior exhibited in Figs. 4(a) and 4(b) for $x_0 \gtrsim 100\ \mu$m is in agreement with results obtained by Murphy and Aamodt and predicted by the one-dimensional theory.[11]

It was thus concluded that our fast detector unit was capable of measuring the fundamental mirage effect physics of the system without altering the nature of the frequency-domain signals to any measurable extent, with only slight deviations from linearity due to the onset of saturation at pump laser powers in excess of 0.6 W.

II. FM TIME DELAY DOMAIN SIGNAL ANALYSIS

Following the characterization of our photothermal beam deflection apparatus, a swept wave was generated in the HP 3325A synthesizer from dc ($f_1 = 0$) to $f_2 = 1280$ Hz with $T = 0.41$ s, sweep rate $S = 3.122$ kHz/s, and applied to the A/O modulator. Little difference in the time delay domain signals was observed between outputs generated using sinusoidal and square wave modulation, with the latter exhibiting somewhat better coherence than the former. Therefore, for all subsequent experimentation swept square waves were used as shown in Fig. 5. This, and all subsequent time delay domain experiments were performed with an Ithaco 1201 low noise pre-amp (#17 in Fig. 1) with a bandwidth 10 Hz–300 kHz. The magnitude roll off of the excitation signal at the long time end of the swept ramp is due to the window shape which was superimposed on the frequency domain structure of the swept wave. The window function is used to diminish the importance of high-frequency components outside the useful sweep range Δf, which would tend to distort the output signal. In our experiments a raised Hanning weighting function (i.e., cosine to the fourth power window)[14] was used over the frequency spectrum of the PDS signals. Therefore, the responses obtained in the time delay domain were, in fact, convolutions with the Fourier transform of the window.

The performance of the spectrometer was first assessed on time delay domain responses obtained from PDS phenomena at the anodized aluminum blackbody/water interface. Figure 6 shows the impulse response $h(\tau)$ and the cross-correlation $R_{xy}(\tau)$ functions generated with a beam offset of $\sim 10\ \mu$m, averaged over 1000 frequency sweeps with 1024 data points per sweep. The total amount of time required for each curve in Fig. 6 was approximately 6–7 min. This time could easily be halved or less, as the quality of the spectral functions remained essentially unaltered after 200–300 averages were obtained. Both $h(\tau)$ and $R_{xy}(\tau)$ have essentially the same peak delay time τ_0 and full-width at half-maximum time τ_{FWHM}, with a somewhat longer delay time of the minimum (negative) cross correlation τ_{min} than the impulse response τ_{min}. This small discrepancy may be due to the oscillatory nature of the cross-correlation function about the zero level on either side of the peak.[15] Otherwise, the curves of Figs. 6(a) and 6(b) are essentially identical. Figure 7 shows the autocorrelations of the input (a) and output (b) signals corresponding to the data of Fig. 6. It can be

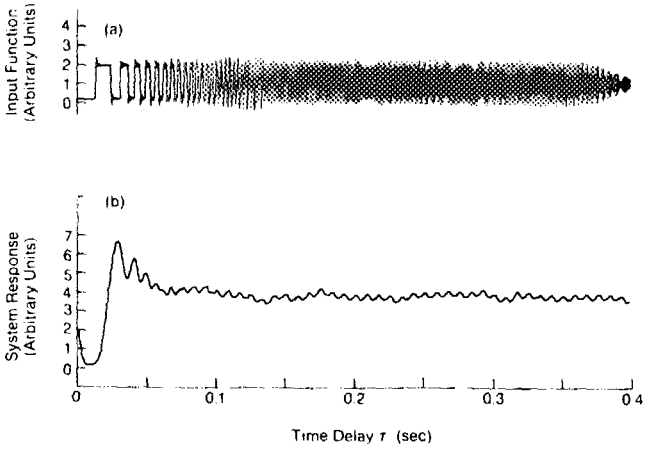

FIG. 5. FM excitation swept square-wave function (a) and PDS response of an anodized aluminum/water interface (b).

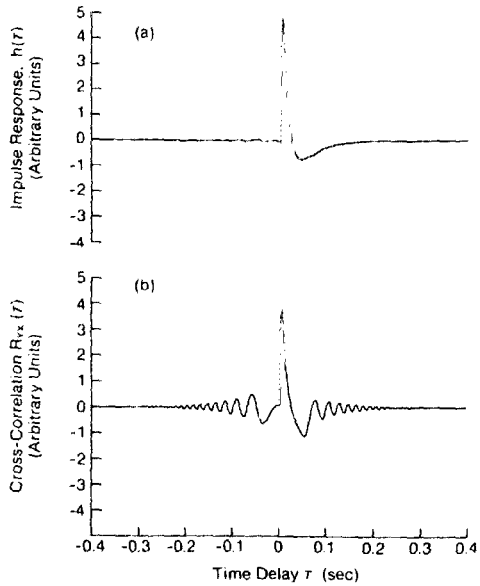

FIG. 6. (a) Impulse response of anodized aluminum/water interface at beam offset $x_0 \cong 50\ \mu$m. Peak delay time $\tau_0 = 2.34$ ms; $\tau_{\text{FWHM}} = 5.13$ ms; $\tau_{\text{min}} = 23.44$ ms. (b) Cross correlation of the same system. Peak delay time $\tau_0 = 2.34$ ms; $\tau_{\text{FWHM}} = 5.2$ ms; $\tau_{\text{min}} = 26.56$ ms.

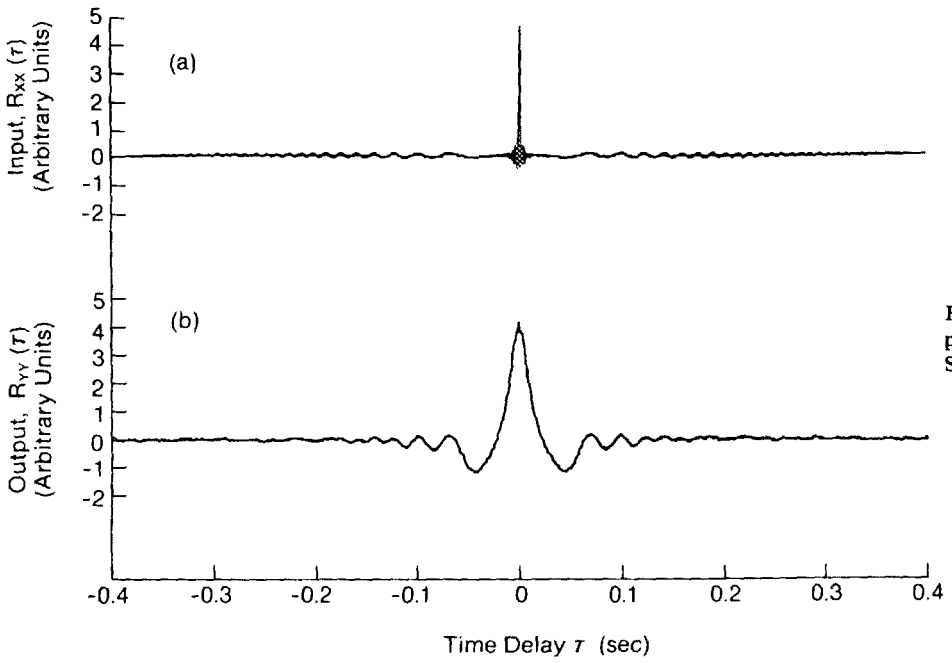

FIG. 7. Autocorrelation functions of (a) the input and (b) the output PDS signal waveforms. Swept wave excitation between dc and 1280 Hz.

observed from Fig. 7(a) that the input autocorrelation $R_{xx}(\tau)$ is extremely narrow on the time scale of the experiment and can, therefore, be approximated by the Dirac delta function

$$R_{xx}(\tau) \cong \delta(\tau) . \tag{10}$$

From Part I we can write

$$R_{xy}(\tau) \cong h(\tau) * \delta(\tau) = h(\tau) \tag{11}$$

in agreement with Fig. 6. The impulse response of Fig. 6(a) can be essentially understood in terms of thermal wave conduction from the blackbody surface into the water mass, after excitation by a thermal pulse of infinitesimal duration at time $\tau = 0$. In that case the spatial and temporal profile of the temperature rise in the fluid is given by the Green's function corresponding to the one-dimensional heat conduction equation. The solution is[16]

$$T_f(x,\tau) = \frac{Qk_s(\alpha_f/\alpha_s)^{1/2}}{(k_s\alpha_f^{1/2} + k_f\alpha_s^{1/2})} \frac{\exp(-x^2/4\alpha_f\tau)}{(\pi\tau)^{1/2}}, \tag{12}$$

where a plane instantaneous heat source of strength Q (J/cm^2) was assumed in the solid at its surface, the solid–liquid interface, at $x' = 0$. Using the paraxial ray Eq. (6) and a time-delay domain Taylor expansion for the fluid refractive index similar to Eq. (7), we can write the equation of motion of the probe beam intensity centroid deflection (see Fig. 1)

$$\frac{d^2x_a}{dz^2}(\tau,z) + \frac{F}{\tau^{3/2}} x_a(\tau,z)\exp[-x_a^2(\tau,z)/4\alpha_f\tau] = 0 , \tag{13}$$

where

$$F \equiv \frac{1}{2} Q\left(\frac{\partial n}{\partial T}\right)_{T=T_0} \frac{k_s}{n_0(\pi\alpha_s\alpha_f)^{1/2}(k_s\alpha_f^{1/2} + k_f\alpha_s^{1/2})} . \tag{14}$$

Equation (13) is nonlinear and can be solved analytically only via a perturbation analysis[12] in the delay time regime

$$\zeta \equiv Fx_0/\tau^{3/2} < 1/x_a , \tag{15}$$

i.e., for

$$\tau > (Fx_ax_0)^{2/3} . \tag{16}$$

For our experiments the time range suggested by Eq. (16) is $(Fx_ax_0)^{2/3} \sim 0$ (10^{-4} s), thus a perturbation expansion of the form

$$x_a(\tau,z) = \sum_{k=0}^{\infty} \zeta^k X_k(\tau,z) \tag{17}$$

was assumed valid. Keeping terms up to first order in ζ only yields

$$x_a(\tau,z) = x_0[1 - (Fz^2/2\tau^{3/2})e^{-x_0^2/4\alpha_f\tau}] . \tag{18}$$

Equation (18) predicts a peak delay time

$$\tau_0 = x_0^2/6\alpha_f . \tag{19}$$

Using $x_0 = 50$ μm and[1] $\alpha_f = 1.4\times10^{-3}$ cm^2/s, one finds $\tau_0 = 2.97$ ms in good agreement with the experimental τ_0, Fig. 6, in view of the uncertainty inherent in the determination of x_0 and the approximations involved in the derivation of Eq. (19). (Note: experimentally τ_0 was printed out directly from the FFT analyzer. A cursor was moved over the display in small steps to select the peak channel; this can be done precisely because the display is derived from a large number of channels. Figure 6 is a copy of the display.) In fact, the experimental τ_0 can be used to calculate x_0 from Eq. (19) more accurately than the positioning micrometers and direct observation are capable of ($x_0 = 44\,\mu$m from the value $\tau_0 = 2.34$ ms calculated from Fig. 6). Equation (18) can be also used to compute the FWHM in Fig. 6

$$x_a(\tau_{\mathrm{FWHM}},z) = \tfrac{1}{2}x_a(\tau_0,z) . \tag{20}$$

It can be shown that

$$\tau_{\mathrm{FWHM}} \cong x_0^2/(4\ln 2)\alpha_f , \tag{21}$$

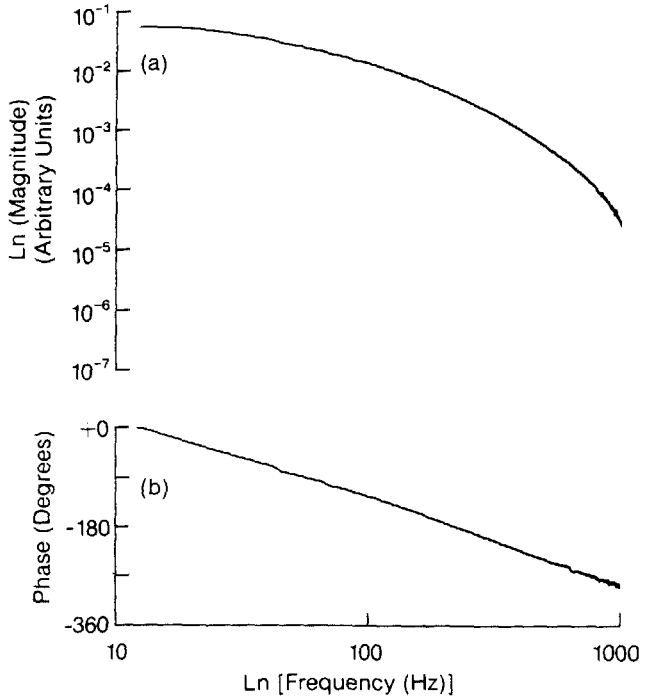

FIG. 8. Magnitude (a) and phase (b) of the complex transfer function $H(f)$ of the blackbody/water interface. Pre-amp bandwidth range 10 Hz–300 kHz. Figure 2 is this figure's counterpart using dispersive lock-in detection.

provided that $\tau_0 \ll (e^{-3/2} F z^2/2)^{2/3}$. Numerically, Eq. (21) gives $\tau_{\mathrm{FWHM}} = 4.99$ ms in good agreement with the experimental τ_{FWHM} in Fig. 6. The trough observed in the impulse response and the cross-correlation function past the zero-crossing delay time cannot be explained by heat diffusion consideration alone. Jackson *et al.*[6] have observed a similar negative response in a PDS pulsed laser experiment, in which the absorbed optical pulse from a pulsed dye laser in 0.1% benzene in distilled CCl_4 acted as an instantaneous heat source in the fluid. The trough has also been observed by other workers photoacoustically.[17,18] It has been explained theoretically in terms of a pressure wave rarefaction following a strong compression in the fluid due to a pulsed heat source of short duration.[19]

The system response obtained in Figs. 6 and 7 indicates that our FM time delay mirage effect apparatus generates the equivalent of a thermal impulse relaxation during the delay times of the measurements. The signal profiles $h(\tau)$ and $R_{xy}(\tau)$ are mathematically the one-dimensional heat diffusion Green's functions of the blackbody/water system with a fluid pressure wave superposed at $\tau \gg \tau_0$. Another important feature of our spectrometer is its ability to calculate and plot on the screen of the FFT analyzer the magnitude and phase of the complex transfer function of the system [see Part I, Eqs. (28)–(31)] in an amount of time equal to a frequency sweep time T. The total experimental time required for such a display (Fig. 8) can be as low as 1 min, corresponding to a minimum number of ~200 sweeps/average. This time is far shorter than the time required to obtain the same information dispersively using lock-in detection, Figs. 2(a) and 2(b). This characteristic is by no means unique to FM time delay systems, but rather common to random noise signals.[20] The superior dynamic range properties of this technique, however, when compared to other random noise methods render it most reliable for fast frequency response measurements on time scales desirable for thermal mapping or depth profiling applications in environments requiring fast turn-around, such as industrial laboratories.

III. THIN LAYER MEASUREMENTS

The spectrometer was further used to measure the response from thin microscope quartz slide layers in direct contact with the backing material (anodized aluminum support). The back side of the slides was painted with black paint, which was allowed to dry out after contacting the backing in order to avoid interfacial thermal resistances due to air gaps, water seepage, etc. Such resistances could alter the temporal profile features of the response.[21] A single slide cut in many pieces was used for these experiments, to assure material uniformity. Each piece was etched in 50% HF:50% H_2O down to the desired thickness. Figure 9 shows a superposition of the impulse responses for two different thicknesses, 30 μm (curve a) and 100 μm (curve b). The cross-correlation functions show similar features, i.e., an increased peak delay time, a broadened FWHM, and an increased trough time delay τ_{min} with increasing thickness. In each case data were taken at beam offset positions which maximized the PDS output at the detector.

The secondary oscillations on both wings of the main pulse in Fig. 9 are consistent with thermal energy arrivals at the sample surface after multiple reflections at the sample-backing interface. The delay time $\Delta\tau$ between two successive peaks corresponds roughly to twice the thermal transit time $\tau_{\mathrm{transit}} = l^2/\alpha_2$ through the bulk of the sample. Similar effects have been predicted theoretically by Burt[22] in fluids excited by pulsed lasers and have been observed experimentally in liquids and solids by Tam *et al.*[23,24]

Figure 10 shows plots of τ_0, τ_{FWHM}, and τ_{min} for the system impulse response as functions of glass layer thickness. A theoretical model based on an extension of the solid–

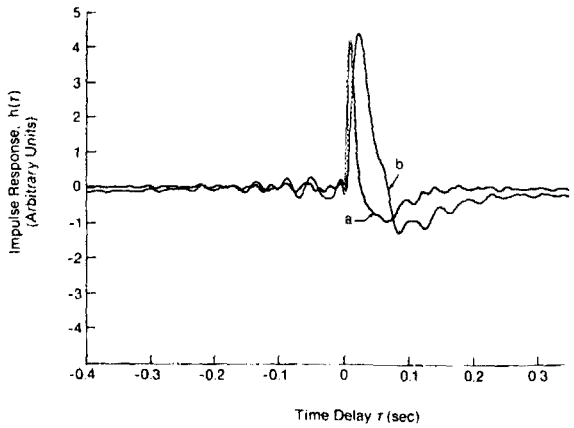

FIG. 9. Impulse response functions from quartz layers of thickness 30 μm (a) and 100 μm (b). $\tau_0^a = 4.69$ ms, $\tau_{\mathrm{FWHM}}^a = 6.04$ ms, $\tau_{\mathrm{min}}^a = 32.81$ ms; $\tau_0^b = 10.94$ ms, $\tau_{\mathrm{FWHM}}^b = 28.6$ ms, $\tau_{\mathrm{min}}^b = 42.97$ ms.

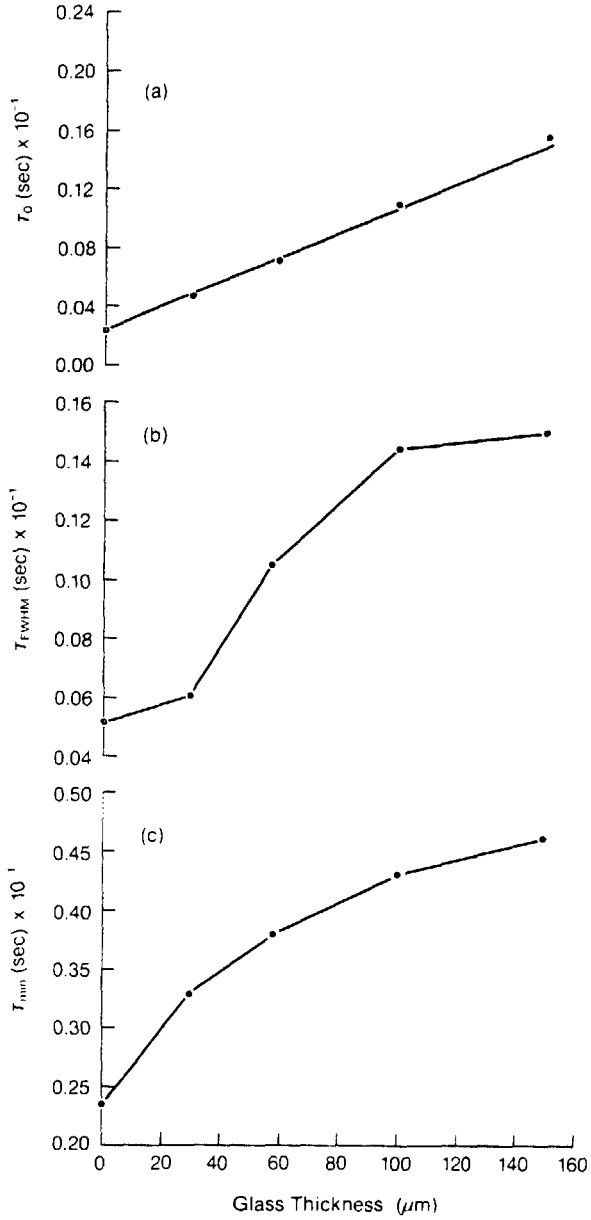

FIG. 10. Impulse response parameters vs microscope slide quartz thickness: (a) $\tau_0(l)$; (b) $\tau_{FWHM}(l)$; (c) $\tau_{min}(l)$.

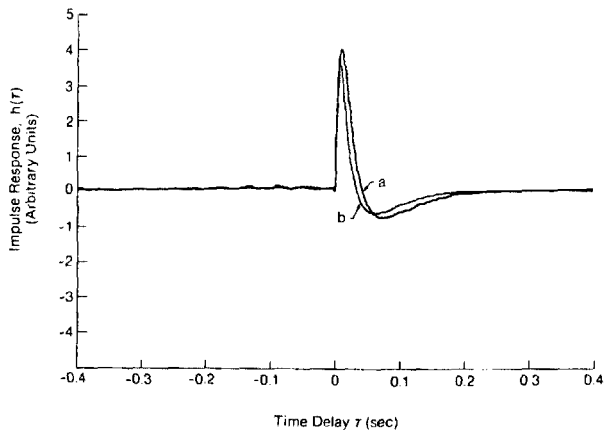

FIG. 11. Impulse responses from (a) Si and (b) SiO_2/Si. $\tau_0^a = 4.3$ ms; $\tau_{FWHM}^a = 10.42$ ms; $\tau_{min}^a = 37.5$ ms; $\tau_0^b = 3.12$ ms; $\tau_{FWHM}^b = 7.64$ ms; $\tau_{min}^b = 31.64$ ms. Traces (a) and (b) are the averages of 1000 responses.

liquid interface heat conduction model of the previous section was developed in the Appendix and used to interpret the results of Fig. 10(a). No attempt was made at interpreting Figs. 10(b) and 10(c) due to the fluid pressure fluctuation phenomena which are likely[19] to dominate them beyond the peak delay time regimes, on which τ_{FWHM} and τ_{min} depend strongly. From Eq. (A13) the peak delay time can be written

$$\tau_0(l) = (L_0^2/6\alpha_3)[1 + (\alpha_3/\alpha_2)^{1/2}(l/L_0)]^2 . \quad (22)$$

For geometries such that

$$(\alpha_3/\alpha_2)^{1/2} l \ll L_0 , \quad (23)$$

Eq. (22) gives the approximate expression

$$\tau_0(l) \cong [1 + 2(\alpha_3/\alpha_2)^{1/2}(l/L_0)] . \quad (24)$$

In our experiments, assuming the validity of Eq. (23), a linear dependence of τ_0 on l would be predicted. From a least-squares fit of Fig. 10(a) to a straight line, the intercept $\tau_0(0)$ gives $L_0 = 44.3\,\mu$m and the slope

$$\frac{\partial \tau_0(l)}{\partial l} \equiv \Delta = \frac{L_0}{3(\alpha_2\alpha_3)^{1/2}} \quad (25)$$

can be used to calculate α_2

$$\alpha_2 = (1/\alpha_3)(L_0/3\Delta)^2 \cong 4\times 10^{-3}\ \text{cm}^2/\text{s} \quad (26)$$

in good agreement with the published value[1] of 4.4×10^{-3} cm^2/s for the thermal diffusivity of quartz. Using the experimental values for α_2 and L_0, a check on Eq. (23) shows that this condition is approximately satisfied for sample thicknesses smaller than $100\,\mu$m, which is thus consistent with the observed linear dependence of τ_0 on l.

Further tests of the sensitivity of our apparatus were performed on a silicon wafer of ~ 300-μm thickness. Half of the wafer had a 1-μm field SiO_2 grown. Figure 11 shows the impulse responses obtained from both sides of the Si/SiO_2 interface. Trace (a) is broader than trace (b) and corresponds to the crystalline Si response. The sensitivity of the spectrometer is thus shown to be high enough to resolve the 1-μm SiO_2 layer. Qualitatively, the SiO_2 layer absorbs more efficiently the 1.06-μm incident radiation than the essentially transparent crystalline Si layer. Therefore, the SiO_2/Si system is expected to generate the equivalent of a pulsed thermal source closer to the surface than the Si wafer. The thermal pulse released to the overlying water medium from the SiO_2/Si structure will thus be narrower and will peak earlier than that from Si, in agreement with Fig. 11.

APPENDIX: THERMAL IMPULSE MIRAGE EFFECT RESPONSE OF A COMPOSITE SYSTEM (TWO SOLIDS)

The system geometry is shown in Fig. A1. To obtain a Green's function representation for the heat conduction problem in the transparent sample (2) following an instantaneous thermal impulsive excitation of unit strength at $x = x'$ at $\tau = 0$ in the blackbody backing (1), the tempera-

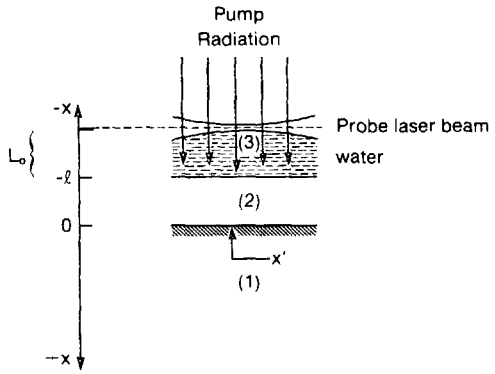

FIG. A1. One-dimensional geometry of Green's function treatment of the PDS problem in the time delay domain. (1) Blackbody backing; (2) thin transparent quartz layer; (3) water.

ture in region (1) can be written[16]

$$T_1(x,\tau) = u_1(x,\tau) + w_1(x,\tau)\,, \tag{A1}$$

where

$$u_1(x,\tau) = (1/2\sqrt{\pi\alpha_1\tau})e^{-(x-x')^2/4\alpha_1\tau} \tag{A2}$$

and

$$\bar{w}_1(x,s) = Ae^{-q_1 x}\,; \quad x>0\,. \tag{A3}$$

Barred quantities indicate Laplace transforms, s is the Laplace domain variable, and $q_i \equiv (s/\alpha_i)^{1/2}$. A is a constant to be determined from boundary conditions. Thus, in region (1)

$$\bar{T}_1(x,s) = (1/2\alpha_1 q_1)e^{-q_1|x-x'|} + Ae^{-q_1 x}\,; \quad x>0\,. \tag{A4}$$

Similarly, in region (2) we can write

$$\bar{T}_2 = \bar{w}_2(x,s) = Be^{q_2 x} + Ce^{-q_2 x}\,; \quad l\leqslant x\leqslant 0 \tag{A5}$$

and in region (3)

$$\bar{T}_3 = \bar{w}_3(x,s) = De^{q_3(x+l)}\,; \quad x\leqslant -l\,. \tag{A6}$$

Equations (A4)–(A6) can be solved simultaneously, subject to boundary conditions of temperature and heat flux continuity at each interface $x=0$ and $x=-l$, and the constants A, B, C, D can be uniquely determined. Experimentally, we are only interested in the expression for the constant D, as it is within region (3) that the PDS signal is generated. For our experimental situation of a heat source creation at the surface of the blackbody backing material due to absorption of the incident Nd^{3+}:YAG laser power, we can set $x'=0$ in Eq. (A4). After some algebraic manipulation the expression for the Laplace transform of the temperature in the fluid region (3) is

$$\bar{T}_3(x,s) = \frac{2be^{q_3(x+l)}}{\alpha_1 q_1[(b+1)(g+1)e^{q_2 l} - (b-1)(g-1)e^{-q_2 l}]}\,, \tag{A7}$$

where

$$b \equiv k_1\alpha_2^{1/2}/k_2\alpha_1^{1/2} \tag{A8}$$

and

$$g \equiv k_3\alpha_2^{1/2}/k_2\alpha_3^{1/2}\,. \tag{A9}$$

Assuming material properties such that

$$k_1\alpha_2^{1/2} \approx k_2\alpha_1^{1/2}\,, \tag{A10}$$

i.e., $b\cong 1$, Eq. (A7) can be simplified considerably

$$\bar{T}_3(x,s) = \frac{2k_1k_2(\alpha_2\alpha_3)^{1/2}e^{-q_2 l + q_3(x+l)}}{(\alpha_1 s)^{1/2}(k_1\alpha_2^{1/2} + k_2\alpha_1^{1/2})(k_3\alpha_2^{1/2} + k_2\alpha_3^{1/2})}\,. \tag{A11}$$

The Laplace transform (A11) can be inverted directly[16] to yield

$$T_3(x,\tau) = \frac{2k_1k_2(\alpha_2\alpha_3/\alpha_1)^{1/2}}{(k_1\alpha_2^{1/2} + k_2\alpha_1^{1/2})(k_3\alpha_2^{1/2} + k_2\alpha_3^{1/2})} \times \frac{\exp\{-[(\alpha_3/\alpha_2)^{1/2}l + |x+l|]^2/4\alpha_3\tau\}}{(\pi\tau)^{1/2}}\,. \tag{A12}$$

Equation (A12) is similar in form to Eq. (12) and, therefore, when subjected to the paraxial ray approximation perturbation analysis which follows Eq. (12) it predicts the following peak delay time for the system of Fig. A1:

$$\tau_0 = [(\alpha_3/\alpha_2)^{1/2}l + L_0]^2/6\alpha_3 \tag{A13}$$

where

$$L_0 \equiv -x-l\,, \tag{A14}$$

i.e., the sample (2) surface lies at $L_0=0$ and, thus, L_0 is the beam offset above the sample surface.

[1] A. Rosencwaig, in *Photoacoustics and Photoacoustic Spectroscopy*, Chemical Analysis (Wiley, New York, 1980), Vol. 57.
[2] Brüel and Kjaer, in *Condenser Microphone Cartridges*, Product Data, 1985, DK-2850 Naerum, Denmark.
[3] A. Mandelis and B. S. H. Royce, J. Appl. Phys. **51**, 610 (1980).
[4] A. Mandelis and J. T. Dodgson, J. Phys. C (in press).
[5] Y. Sugitani, A. Uejima, and K. Kato, J. Photoacoust. **1**, 217 (1982).
[6] W. B. Jackson, N. M. Amer, A. C. Boccara, and D. Fournier, Appl. Opt. **20**, 1333 (1981).
[7] N. M. Amer, J. Phys. Colloq. **C6**, 185 (1983).
[8] United Detector Technology, Hawthorne, CA; UDT 431 X-Y Optical Position Indicator.
[9] M. M. Farrow, R. K. Burnham, M. Auzanneau, S. L. Olsen, N. Purdie, and E. M. Eyring, Appl. Opt. **17**, 1093 (1978).
[10] N. J. Dovichi, T. G. Nolan, and W. A. Weimer, Anal. Chem. **56**, 1700 (1984).
[11] J. C. Murphy and L. C. Aamodt, J. Appl. Phys. **51**, 4580 (1980).
[12] A. Mandelis and B. S. H. Royce, Appl. Opt. **23**, 2892 (1984).
[13] A. Mandelis, J. Appl. Phys. **54**, 3404 (1983).
[14] H. Biering and O. Z. Pedersen, Brüel Kjaer Tech. Rev. **1**, 43 (1983).
[15] J. S. Bendat and A. G. Piersol, in *Engineering Applications of Correlation and Spectral Analysis* (Wiley, New York, 1980), Chap. 3.
[16] H. S. Carslaw and J. C. Jaeger, in *Conduction of Heat in Solids*, 2nd ed. (Clarendon, Oxford, 1959), Chap. XIV.
[17] B. Sullivan and A. C. Tam, J. Acoust. Soc. Am. **75**, 437 (1984).
[18] C-Y. Kuo, M. F. Vieira, and C. K. N. Patel, J. Appl. Phys. **55**, 3333 (1984).
[19] H. M. Lai and K. Young, J. Acoust. Soc. Am. **72**, 2000 (1982).
[20] H. Coufal, J. Photoacoust. **1**, 413 (1983).
[21] A. Uejima, D. Curtis, and Y. Sugitani, J. Photoacoust. **1**, 397 (1983).
[22] J. A. Burt, J. Phys. D **13**, 1985 (1980).
[23] A. C. Tam and C. K. N. Patel, Appl. Opt. **18**, 3348 (1979).
[24] H. Sontag and A. C. Tam, Appl. Phys. Lett. **46**, 725 (1985).